

# A Coupled Rate Theory-Monte Carlo Model of Helium Bubble Evolution in Plasma-Facing Micro-Engineered Tungsten

Edward Gao, Nasr M. Ghoniem

*Department of Mechanical & Aerospace Engineering, University of California, Los Angeles (UCLA),  
420 Westwood Plaza, Los Angeles, CA. 90095-1597, U.S.A.*

---

## Abstract

A multiscale model of helium bubble evolution in plasma-facing materials is developed. The model links different stages of helium bubble evolution: deposition, nucleation, growth, motion, and coalescence. Helium deposition is simulated with the SRIM Monte Carlo program to give spatial information on helium and displacement damage distributions near the surface. This deposition profile is then introduced into a space-dependent rate theory of bubble nucleation and growth to describe the early stages of the distribution and size of helium bubbles. The coarsening stage of bubble evolution as a result of whole bubble motion, interaction, and coalescence is modeled by a new Object Kinetic Monte Carlo (OKMC) model, for which initial conditions are taken from the mean-field rate theory calculations. The model is compared to experimental data on low-energy helium plasma interaction with micro-engineered tungsten (W), and on high-energy helium ion deposition in flat W samples. Novel features of the multiscale model include: (1) space-dependent rate theory; (2) OKMC model of bubble motion in stress and temperature fields; and (3) application of the model to micro-engineered materials, and comparison with experiments on the same time-scale. At low helium ion energy, it is found that the mechanism of trap mutation is essential in achieving good agreement with experimental measurements. On the other hand, good agreement with experiments at high incident ion energy and temperature showed the importance of bubble coalescence and coarsening as main mechanisms. The results of the model are compared with experiments on flat W surfaces irradiated at high ion energy (30 keV), and with micro-engineered W, where the surface is coated with high-density micro-pillars at low ion energy (around 100 eV). The predicted average bubble radius and density are in qualitative agreement with experimental results.

---

---

\*To whom correspondence should be addressed;  
Email: EdwardXiangGao@gmail.com

## Contents

|          |   |           |
|----------|---|-----------|
| <b>1</b> | <b>Introduction</b>                                       | <b>3</b>  |
| <b>2</b> | <b>Multiscale Model Methodology</b>                       | <b>4</b>  |
| 2.1      | Bubble Evolution Overview . . . . .                       | 4         |
| 2.2      | Rate Theory of Early Nucleation & Growth . . . . .        | 6         |
| 2.3      | OKMC Model of Motion and Coarsening . . . . .             | 11        |
| <b>3</b> | <b>Modeling Results &amp; Comparison with Experiments</b> | <b>15</b> |
| 3.1      | Helium Ion Deposition . . . . .                           | 15        |
| 3.2      | Spatial Rate Theory Results . . . . .                     | 15        |
| 3.3      | OKMC Simulations of Low-Energy Helium Ions . . . . .      | 17        |
| 3.4      | OKMC Simulations of High-Energy Helium Ions . . . . .     | 21        |
| <b>4</b> | <b>Conclusions</b>  | <b>23</b> |

## 1. Introduction

As we move closer to the realization of fusion energy, the reliability of structural materials becomes a major concern. One of the structural components that operates in the severest of environments is the Divertor of present and future Tokamak-type reactors, where extreme levels of heat and particle fluxes are expected to impinge on its surface. Currently, a leading candidate structural material for the divertor application is tungsten (W), because of its high melting point and considerable thermal conductivity. However, W is brittle at low temperatures and thus must operate at higher temperatures to avoid fracture. Unfortunately, the irradiation of W surfaces with energetic ions from the plasma introduces various defects, which can also reduce the material's overall mechanical strength, even at higher temperatures [1–3]. In addition to the thermo-mechanical damage that high heat and particle fluxes can introduce into the W divertor surface, erosion due to sputtering (both atomic and by generating dust and flakes) is also a factor in limiting the Divertor lifetime. Massive surface erosion can result from changes in the surface structure, as nano-scale helium and hydrogen bubbles can lead to surface fuzz and flake formation. The formation of a high density of subsurface bubbles in W can lead to hardening, embrittlement, and reduction of thermal conductivity. When a plasma transient impinges on the surface of a Plasma-Facing Component (PFC), reduced thermal conductivity can lead to additional thermo-mechanical damage. Thus, it is of interest to understand the physics of helium and hydrogen bubble formation near the surface of W structures that are designed to intercept extreme particle and heat fluxes.

The physics of point defects and gas atoms in solids has received considerable attention for some time, because of the enormous implications in designing reliable structures in fission and fusion energy systems. However, the majority of studies focused on the formation of voids, bubbles, Self Interstitial Atom clusters (SIAs) and Stacking Fault Tetrahedra (SFTs) in bulk, neutron-irradiated materials. In PFCs, substantially more helium and hydrogen gas is injected into the surface from the plasma side as compared to gas production from inelastic nuclear collisions and transmutations. Thus, while theories of void and bubble formation in irradiated metals have largely focused on average bulk behavior under conditions of relatively low rates of gas production from nuclear collisions, the situation in PFCs is quite different. First, the rates of gas production via plasma implantation is several orders of magnitude higher than in bulk structural materials, like the first wall. Second, the proximity of implanted helium and hydrogen to the surface makes it imperative to model not only the temporal evolution of bubbles, but their spatial distribution as well. Finally, the severe temperature and stress gradients near the surface allows whole bubbles to move, coalesce and form larger surface perforations as they exit. It is thus clear that traditional mean field rate theory of void and bubble swelling is not adequate to describe the full evolution of gas bubbles in PFCs. Moreover, since nucleation of these bubbles starts at the nano-scale, while subsequent growth and motion of bubbles must be determined over significant material volumes (at least microns), a multiscale modeling approach is necessary.

Recent advances in material processing have led to the fabrication of W surfaces that are endowed with special architecture. The developed material architecture include reticulated foam with open cells and variable ligament size, as well as uniform conical and cylindrical micropillars [4, 5]. Our experimental work has demonstrated that the spatial distribution of subsurface helium bubbles in these micro-engineered materials is fundamentally different from the corresponding distributions found in flat W surfaces after plasma exposure. To enable physical

understanding of differences in bubble evolution between flat and micro-engineered W surfaces, we develop here a multiscale model that encompasses bubble nucleation, growth, coalescence and spatial redistribution. The model is a hybrid combination of a mean-field rate theory of nucleation and growth, coupled with an Object Kinetic Monte Carlo (OKMC) simulation of post-nucleation bubble motion, coalescence and growth. The multiscale model captures the essential features of temporal and spatial evolution of subsurface bubbles in PFCs, and sheds considerable light on the physics of bubble evolution in PFCs with micro-engineered surface features. The numerical results of this model are compared to our recent experimental observations on low energy (100 eV) helium plasma exposure performed at UCSD’s PISCES-B facility [5]. We make further comparisons between the model and high energy helium implantation experiments (30 keV) performed at the University of Wisconsin [6].

The paper is organized as follows. In section 2, we present details of the theoretical development of the multiscale model and the procedures of its numerical implementation, while the results are presented in section 3, with discussions of the key mechanisms unveiled by comparing the model to experiments. Finally, conclusions are given in section 4.

## **2. Multiscale Model Methodology**

### *2.1. Bubble Evolution Overview*

Helium accumulation in the subsurface region of tungsten exposed to an incident helium plasma ion flux proceeds through a number of steps, as outlined by Trinkaus and Singh [7]. The distinct stages of bubble formation include the processes of implantation, nucleation, growth, and finally coarsening. Helium ion implantation is a very fast process, and is a result of the penetration of energetic helium to the surface, followed by energy loss in electronic and atomic collisions, finally the generation of a cascade of collisions that result in the displacement of atoms, the creation of Frenkel Pairs (FPs), and the deposition of a neutral helium atom in an interstitial or substitutional position in the crystal lattice. Bubble nucleation commences immediately after this stage, where the diffusion of helium atoms and FPs result in the condensation of clusters of helium and vacancies to form nascent bubbles. The critical nucleus for bubble formation under the conditions of high helium generation or implantation rates has been shown to be small, on the order of 3 atoms. This will be important in simplifying the clustering model of nucleation and growth that will be discussed later. Meanwhile, during low energy exposures, helium ions irradiations do not create FPs. In such case, the clustering of helium as extrinsic interstitials forcibly create FPs via the self-trapping mechanism [8]. As helium continues to be implanted, fresh helium atoms and vacancies will be attracted towards the small helium bubbles, and such bubble nuclei continue to grow. This process takes place simultaneously with the nucleation of new bubbles. Thus, existing bubbles grow in competition with the formation of new bubbles. Similarly, for low energy exposures that lack irradiation vacancies, FPs are created through trap-mutation, which will be discussed in the following section.

At some helium concentration, it becomes more probable that additional helium and vacancies would be absorbed on existing helium bubbles than nucleating new bubbles in the matrix. Therefore, growth of existing bubbles takes over, and the bubble density does not change much for a while. We developed a mean-field theory of simultaneous nucleation and growth that we will extend here to treat spatial effects specific to helium implantation from the plasma. As bubbles continue to grow, they are subjected to additional forces resulting from stress and temperature gradients, and will be buffeted by stochastic helium and vacancy fluxes as well. Thus,

entire bubbles can move, either randomly as a result of stochastic FP and helium fluxes, or directed by stress and temperature gradients. When bubbles meet one another, they coalesce and grow to significantly larger sizes at the expense of their density. This process is described as the bubble coalescence stage, and is characterized by rapid growth, motion of bubbles towards the surface, and a reduction of the bubble density over time. We will introduce these events in an Object Kinetic Monte Carlo (OKMC) model that will be coupled with the rate theory nucleation/growth model described above. A sketch of the various physical processes that are included in the multiscale model is shown in Figure 1. A flowchart of the entire components of the multiscale model is shown in Figure 2, where the implantation phase is simulated with the SRIM binary collision Monte Carlo code [9], the nucleation/growth stage is modeled with an extension of the mean-field rate theory [10, 11], and finally the coalescence and motion stage is modeled with a new OKMC code that we developed specifically for plasma-implanted helium, following our own earlier work [12, 13]. The absorption of helium atoms and vacancies leading to bubble growth can be represented by a set of size distribution equations relating to each species. However, since the size distribution is nearly uniform during early nucleation, it is treated with its mean value in rate equations. OKMC simulations, however, result in a non-uniform size distribution as bubbles grow to significant sizes.

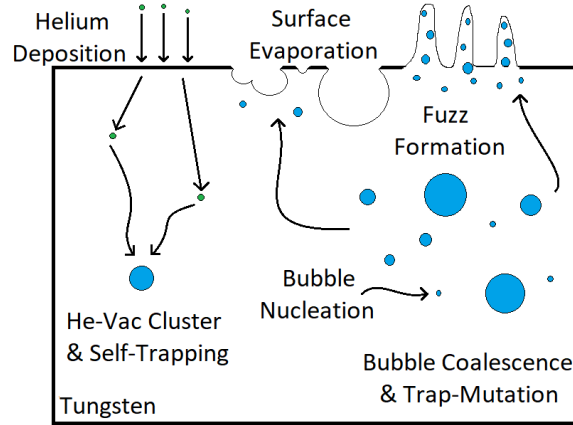


Figure 1: Overview of bubble evolution as helium (green) ions penetrates the tungsten surface to form subsurface gas bubbles (blue) due to trapping effects that eventually return to the surface as micro-scale perforations and tendrils (fuzz).

Our recent experimental work on low-energy helium plasma ion interaction with micro-engineered W surfaces revealed the significance of the local surface geometry in modifying the formation process of helium bubbles in the near-surface region [5]. Micro-engineered W surfaces were prepared with the Chemical Vapor Deposition process as dense arrays of surface micro-pillars of size 4-10  $\mu\text{m}$  in diameter and 20  $\mu\text{m}$  in height. The small size of these micro-pillars did not disturb the electrostatic potential in the plasma edge region, because the surface feature size was much smaller than the Debye shielding length ( $\mu\text{m}$  compared to mm). Therefore, incident low energy plasma ions do not change their direction as they come near the materials surface, and will interact ballistically with surface features, as shown in Figure 3. Thus, in order to differentiate planar tungsten from micro-pillar tungsten, the ion angle of incidence is implemented in the present model as an additional controlling parameter during the implantation stage. Where a planar surface will always be under normal incidence ( $\theta = 0^\circ$ ), the angle will vary on tungsten pillar sides from  $15^\circ$  to near  $90^\circ$ . This concept is illustrated in

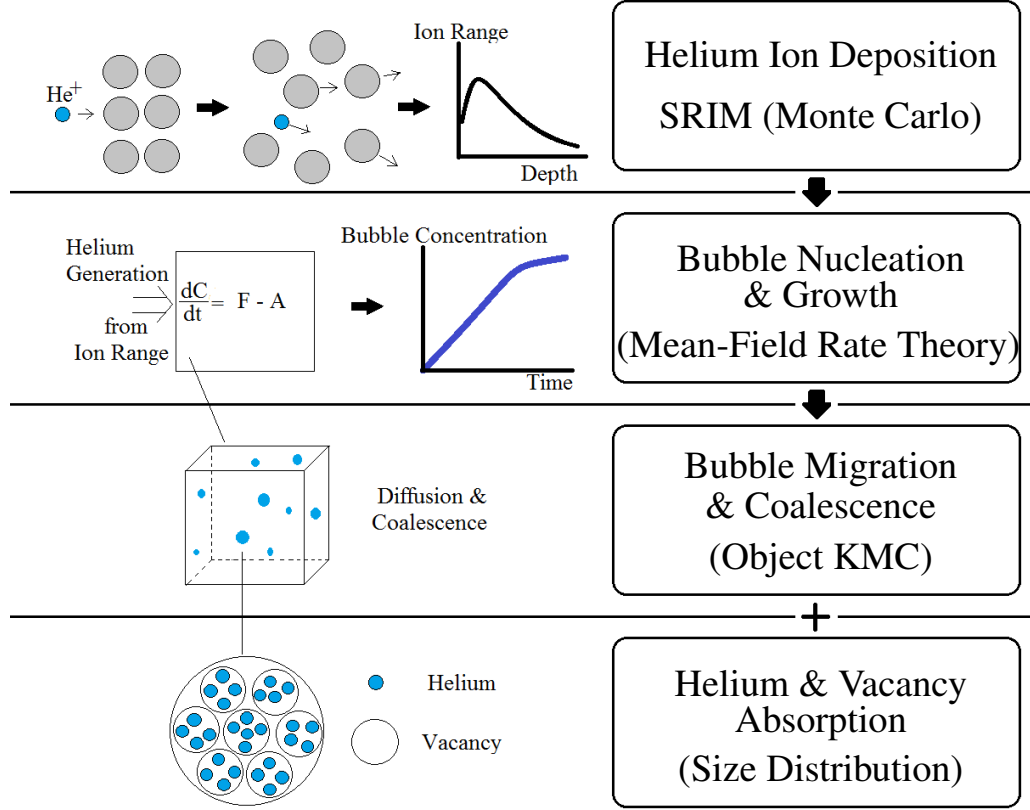


Figure 2: Flowchart of the multiscale bubble evolution model with four stages.

Figure 3. In the following, we describe the present multiscale approach, where we utilize SRIM to model helium implantation in micro-engineered W. The SRIM code, which is based on the binary collision approximation, takes as input helium ions at specific energy and angle of incidence, performs Monte Carlo simulations, and computes the implantation depth, backscattering percentage, and vacancy implantation rate. This is followed by a description of the spatially-dependent rate theory to model bubble nucleation and growth. A new OKMC model is developed to treat the processes of motion, coalescence and further growth of nucleated bubbles near the W surface.

## 2.2. Rate Theory of Early Nucleation & Growth

Classical nucleation theory is inadequate for modeling helium bubble nucleation because of its high sensitivity to physical parameters, which are typically not known to a high degree of accuracy. This aspect renders it virtually non-predictive. In addition, the theory calculates nucleation rates but does not predict defect cluster density nor size as function of irradiation dose. On the other hand, the mean field void growth theory presented above assumes that defect clusters (e.g. voids, bubbles, and dislocation loops) have already nucleated and that their concentrations are constant, independent of dose and spatial location within the material. To remedy these deficiencies and at the same time have a tractable system of cluster dynamics equations, Ghoniem, et al. [10] developed a minimal set of cluster dynamics equations, where assumptions can be made about nucleation of bubbles under high rates of gas production due to nuclear reactions. In this method, a list of coupled rate-equations for the concentrations

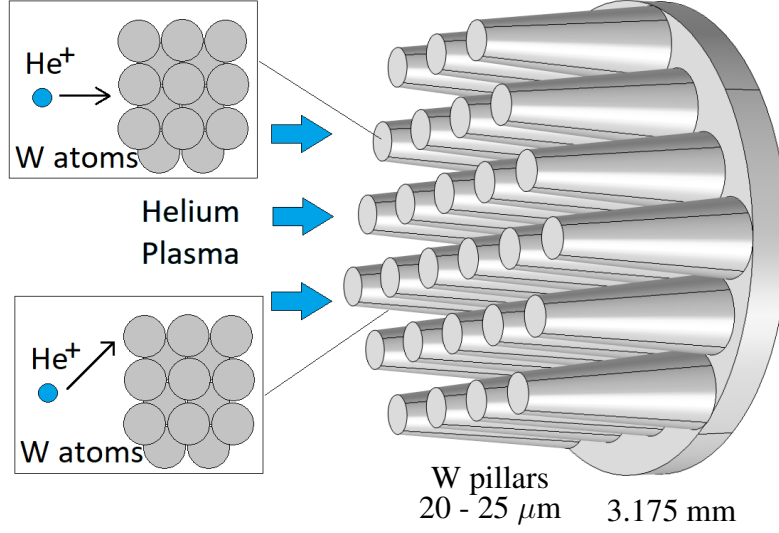


Figure 3: Sketch of helium ion interaction with a micro-engineered tungsten pillar sample showing the different angles of ion incidence between pillar tips and their sides.

of species is developed. Each equation represents a mass balance equation for a particular defect cluster specie as the sum of all production and loss rates of the specie to be equal to its concentration rate of change. Under the mean-field approximation, where statistical variations in time and space are averaged, these equations are only time-dependent. The general structure of the cluster dynamics equations reads:

$$\partial_t C_{ij} + \nabla \cdot \mathbf{J}_{ij} = S_{ij} - L_{ij} \quad (1)$$

The volumetric concentration of a cluster containing  $i$  Frenkel pairs (negative  $i$  for interstitials, and positive  $i$  for vacancies) and  $j$  helium atoms is  $C_{ij}$ , its flux  $\mathbf{J}_{ij}$  is composed of two terms: a diffusive flux  $-D_{ij} \nabla C_{ij}$ , and a convective flux  $\mathbf{V}_{ij} C_{ij}$ , where the velocity  $\mathbf{V}_{ij}$  is proportional to a configurational force  $\mathbf{F}_{ij} = -\nabla E_{ij}$ , where  $E_{ij}$  is an elastic interaction energy, and the proportionality parameter (mobility) is  $M_{ij} = \frac{D_{ij}}{kT}$ . The configurational forces on clusters that lead to convective motion are neglected in the early-stage rate theory, since random motion of single defects (helium, vacancies, and interstitials) is dominant. Brownian motion of larger size clusters is also neglected in the rate theory because of their much lower mobility as compared to single mobile defects. The source and loss terms  $S_{ij}$  and  $L_{ij}$  can include the processes of absorption, coalescence, and emission. The system of clustering equations represented by Eq. 1 is very generic and cannot be solved without specific details. In practice, however, SIAs do not associate with helium atoms (energetically unfavorable), and thus negative values of  $i$  result in separate equations for SIAs. Fu and Willaime [14] show that interstitial helium atoms can be weakly trapped by self-interstitial atoms (with a binding energy of about 0.3 eV). However, they also predict that the emission of a self-interstitial atom is energetically favorable for  $n > 4$ , where  $n$  is the number of helium atoms in a cluster. Thus, for positive values of  $i$  (i.e. vacancies), we assume that vacancies agglomerate with helium atoms  $j$  to produce helium-filled bubbles. The practical combination of  $i$  and  $j$  is determined by the nucleation condition for a stable bubble nucleus, which can be quite large if there is not enough gas atoms to stabilize bubbles. However, when the gas generation rate is high (as in fusion energy neutron spectrum),

a critical stable bubble nucleus can have only one vacancy and 2-3 helium gas atoms bound to it. Divacancies may likewise bind several gas atoms to form stable bubble nuclei. Because the concentration of single vacancies is always much higher than that of di- or tri-vacancies, an assumption can be made that the bubble nucleus size contains only one vacancy and 2-3 gas atoms. Once a critical bubble is formed, the *mean-field* or average bubble can be described by a growth equation.

Following Ghoniem et al. [10], rate equations for the concentrations of vacancies ( $C_{10} = C_v$ ), self-interstitials ( $C_{10} = C_i$ ), helium interstitials ( $C_{01} = C_g$ ), helium substitutional atoms ( $C_{11} = C_{gv}$ ), di-helium interstitials ( $C_{02} = C_{2g}$ ), di-helium mono-vacancy ( $C_{12} = C_{2gv}$ ), the critical nucleus ( $C^*$ ), the bubble density ( $C_b$ ), the number of helium atoms in a bubble ( $m_1$ ), and the average bubble radius according to rate theory ( $R_b$ ) can be expressed as rate equations. Because cluster mobility is a very strong function of its size, only single defects (e.g. vacancies, SIAs, and helium interstitials) are considered to be mobile within the short time-scale of rate theory. At later stages of clustering, the concentration of single defects decreases as they get absorbed into bubbles, and whole bubble motion becomes important. The mobility of helium bubbles will be considered in the following section when discussing their migration rates at longer time-scales.

Since the early eighties, atomistic simulations by Wilson et al. [15] demonstrated that helium atoms can cluster with each other without the need for additional vacancies. In fact, it was found that clustered helium atoms produce their own vacancies and nearby self-interstitial defects, if FPs are not available due to irradiation [15]. As few as five interstitial helium atoms can spontaneously produce a lattice vacancy and nearby self-interstitial. An eight-helium-atom cluster gives rise to two such defects, and 16 helium atoms to more than five self-interstitial vacancy pairs. It was noted that self-interstitials prefer to agglomerate on the same “side” of the helium cluster rather than to spread themselves out uniformly. The binding energy of each additional helium atom to these clusters increases with helium concentration and the trap is apparently unsaturable, as schematically shown in Figure 4. Such process is known as “trap mutation” and would continue to occur as long as helium implantation persists. In fact, Evans et al. have shown direct evidence for helium bubble growth in molybdenum by the mechanism of loop punching [16]. More recently, Boisse et. al. estimated the threshold trap mutation energy in W using density functional theory [8]. Similarly, Faney et. al. discovered that the effect eventually equilibrates to roughly 4 helium atoms per vacancy site [17]. To incorporate this growth mechanism into the rate theory model, we constrain bubble growth to the number of helium atoms inside the bubble, if vacancy flow is insufficient. This constraint ensures that there is at least one vacancy for every four helium atoms in a bubble, thus requiring bubble volume to be  $\lceil m_1/4 \rceil \Omega$ .



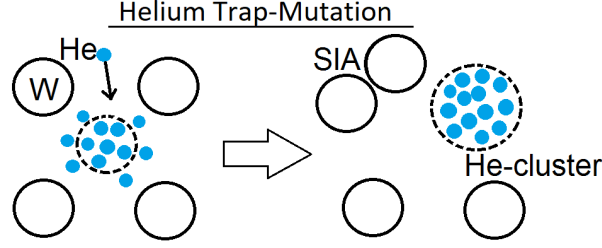


Figure 4: Illustration of the helium trap mutation process, where an existing helium bubble in bulk grows from gas absorption and kick-out of interstitials to the surrounding tungsten lattice in order to relieve internal gas pressure.

Therefore, the *reduced* set of rate equations, derived by Ghoniem et al. [10] is given by:

$$\begin{aligned}
\frac{\partial C_v}{\partial t} &= D_v \nabla^2 C_v + fG + (\beta e_1 + \delta) C_{gv} \\
&\quad - [\alpha C_i + \beta C_g + \gamma (C_s^v + C_{gv} + 2C_{2g} + 2C_{2gv} + 3C^*)] C_v \\
\frac{\partial C_i}{\partial t} &= D_i \nabla^2 C_i + fG - \alpha C_i (C_v + C_{gv} + 2C_{2gv} + 3C^* + C_s^i) \\
\frac{\partial C_g}{\partial t} &= D_g \nabla^2 C_g + G_{He} + \beta (e_1 C_{gv} + e_2 C_{2gv} + 2e_3 C_{2g}) \\
&\quad + \delta (C_{gv} + 2C_{2gv} + 2(2C_{2g}) + 3C^* + m_1 C_b) \\
&\quad + \alpha C_i (C_{gv} + 3C^*) - \beta C_g (C_v + 4C_g + C_{gv} + 2C_{2gv} + 2C_{2g} + 3C^* + \epsilon C_b) \\
\frac{\partial C_{gv}}{\partial t} &= \beta e_2 C_{2gv} + 2\delta C_{2gv} + \beta C_g C_v + 2\gamma C_v C_{2gv} - C_{gv} (\beta e_1 + \delta + \alpha C_i + \beta C_v) \\
\frac{\partial C_{2gv}}{\partial t} &= 3\delta C^* + \beta C_g C_{gv} + 2\gamma C_v C_{2g} - C_{2gv} (\beta e_2 + 2\delta + 2\beta C_v + 2\alpha C_i + 2\gamma C_v) \\
\frac{\partial C_{2g}}{\partial t} &= 2\alpha C_i C_{2gv} + 2\beta C_g^2 - C_{2g} (\beta e_3 + 2\delta + 2\gamma C_v + 2\beta C_g) \\
\frac{\partial C^*}{\partial t} &= 2\beta C_g (C_{2gv} + C_{2g}) - 3C^* (\delta + \alpha C_i + \beta C_g + \gamma C_v) \\
\frac{\partial C_b}{\partial t} &= \frac{1}{m_1} (12\beta C_g C^* + 9\gamma C_v C^*) \\
\frac{\partial m_1}{\partial t} &= \epsilon \beta C_g - \delta m_1
\end{aligned}$$

Along with the average bubble radius either by vacancy flow or trap mutation

$$\frac{\partial R_b}{\partial t} = \begin{cases} \frac{1}{R_b} \left( D_v C_v - D_v C_i - D_v C_v^e \left\{ \exp \left[ \frac{\Omega}{k_B T} \left( \frac{2\gamma_b}{R_b} - p \right) \right] - 1 \right\} \right), & \text{if } \frac{\partial R_b}{\partial t} \geq 0 \\ \left( \frac{\pi \Omega}{16} \right)^{1/3} \frac{\partial m_1}{\partial t}, & \text{otherwise} \end{cases} \quad (2)$$

The original development of Ghoniem et al. [10] did not include spatial distributions of mobile defects nor trap mutation as a condition for bubble growth. In this work, we emphasize the spatial distribution of helium bubbles, extending the original rate theory development, because our experiments showed strong dependence of helium bubble nucleation and growth on the surface structure. In solving this system of equations, other microstructure features (e.g. network dislocations, grain boundaries and precipitates) are assumed to be distributed, and their

interaction rates with point defect and helium-vacancy clusters is taken from the mean-field approximation of rate theory. The reaction frequencies ( $s^{-1}$ ) of self-interstitials ( $\alpha$ ), helium ( $\beta$ ) and vacancies ( $\gamma$ ), and the thermal emission frequencies ( $e_1, e_2, e_3$ ) in the above equations are given as follows [10].  $\alpha = 48\nu_i \exp(-E_i^m/k_B T)$ ,  $\beta = 48\nu_g \exp(-E_g^m/k_B T)$ ,  $\gamma = 48\nu_v \exp(-E_v^m/k_B T)$ ,  $e_1 = \exp(-E_{v,g}^b/k_B T)$ ,  $e_2 = \exp(-E_{v,2g}^b/k_B T)$ ,  $e_3 = \exp(-E_{2g}^b/k_B T)$ , and  $\delta = bG$ . In addition, the diffusion coefficients and factor are  $D_i = (a_0^2/48)\alpha$ ,  $D_g = (a_0^2/48)\beta$ ,  $D_v = (a_0^2/48)\gamma$ ,  $\epsilon = (4\pi/48)(R_b/a_0)$ , while the sink concentrations are  $C_s^v = (a_0^2/48)[Z_v\rho + 4\pi R_b C_b/\Omega]$ ,  $C_s^i = (a_0^2/48)[Z_i\rho + 4\pi R_b C_b/\Omega]$ , and the equilibrium vacancy concentration is  $C_v^e = \exp(-E_v^f/k_B T)$ . The values of all relevant parameters are included in the table below (Table 1).

| Notation      | Parameter                               | Value                    | Unit                 | Reference    |
|---------------|---|--------------------------|----------------------|--------------|
| $a_0$         | Lattice Constant                        | $3.1648 \times 10^{-10}$ | [m]                  | -            |
| $\Omega$      | Atomic Volume                           | $1.5825 \times 10^{-29}$ | [m <sup>3</sup> ]    | -            |
| $E_i^f$       | SIA Formation Energy                    | 9.98                     | [eV]                 | [18–20]      |
| $E_v^f$       | Vacancy Formation Energy                | 3.65                     | [eV]                 | [18–20]      |
| $E_{He}^f$    | Helium Interstitial Formation Energy    | 5.47                     | [eV]                 | [21, 22]     |
| $E_i^m$       | SIA Migration Energy                    | 0.013                    | [eV]                 | [18, 19, 23] |
| $E_v^m$       | Vacancy Migration Energy                | 1.66                     | [eV]                 | [18, 23, 24] |
| $E_{He}^m$    | Helium Migration Energy                 | 0.06                     | [eV]                 | [19, 24, 25] |
| $E_{v,He}^B$  | Helium Substitutional Binding Energy    | 4.57                     | [eV]                 | [18, 23, 25] |
| $E_{v,2He}^B$ | Di-Helium Substitutional Binding Energy | 6.65                     | [eV]                 | [23, 25]     |
| $E_{2g}^B$    | Di-Helium Interstitial Binding Energy   | 1.03                     | [eV]                 | [18, 23, 25] |
| $\nu_i$       | SIA Attempt Frequency                   | $6 \times 10^{12}$       | [Hz]                 | [18]         |
| $\nu_v$       | Vacancy Attempt Frequency               | $6 \times 10^{12}$       | [Hz]                 | [18]         |
| $\nu_{He}$    | Helium Attempt Frequency                | $6 \times 10^{10}$       | [Hz]                 | [18]         |
| <b>b</b>      | Re-solution Parameter                   | 1                        | [1]                  | [10]         |
| <b>f</b>      | Recombination Survival Fraction         | 0.25                     | [1]                  | [26]         |
| $\rho$        | Dislocation Density                     | $3 \times 10^{14}$       | [m/m <sup>-3</sup> ] | [27, 28]     |
| $Z_v$         | Vacancy Bias Factor                     | 1                        | [1]                  | [26, 29]     |
| $Z_i$         | SIA Bias Factor                         | 1.4                      | [1]                  | [26, 29]     |

Table 1: Tungsten material parameters used in rate theory equations.

The internal gas pressure ( $p$ ) is calculated using a virial expansion of the helium equation of state up to the third order:  $p \approx \frac{m_2 k_B T}{V_B} \left( 1 + B \left( \frac{m_2}{N_A V_B} \right) + C \left( \frac{m_2}{N_A V_B} \right)^2 \right)$ , where  $m_2$  is the number of vacancies in the bubble,  $V_B$  the volume of the bubble,  $N_A$  the Avogadro's number, and the virial coefficient ( $B, C$ ) are obtained from references [30–33]. Similarly, the surface tension ( $\gamma_b$ ) is fitted to a linear temperature dependence [34, 35].

The spatial implementation of rate theory utilizes, as input, the results of helium and point defect deposition from SRIM Monte Carlo (MC) binary collision simulations of collision cascades. The spatial distribution of helium and FP generation is determined at this step based on the incident ion energy and angle of incidence, since we are interested in helium deposition in conical micro-pillars. Helium ion deposition is simulated with SRIM at  $\theta = 0^\circ$  ion incidence angle corresponding to planar surfaces, and up to  $\theta = 89^\circ$  corresponding to impingement on the

micro-pillar sides in  $15^\circ$  intervals. A total of  $10^5$  MC iteration steps were carried out for each calculation. The results of SRIM simulations for ion deposition were then fitted to a Gaussian function for the generation rate of helium ( $G_{He}$ ) and FP ( $G$ ) on a tungsten semi-infinite slab surface in the finite element computer program COMSOL Multiphysics (Figure 5). The set of space-dependent rate equations described above is then integrated via the “Partial Differential Equation” module in COMSOL up to 1s of exposure time in  $1 \times 10^{-5}$ s time-steps. Once the bubble concentration reaches steady state (does not vary by more than 10%), the rate theory calculations are stored and used in the next step of the multiscale model with the OKMC method, as will be described next.

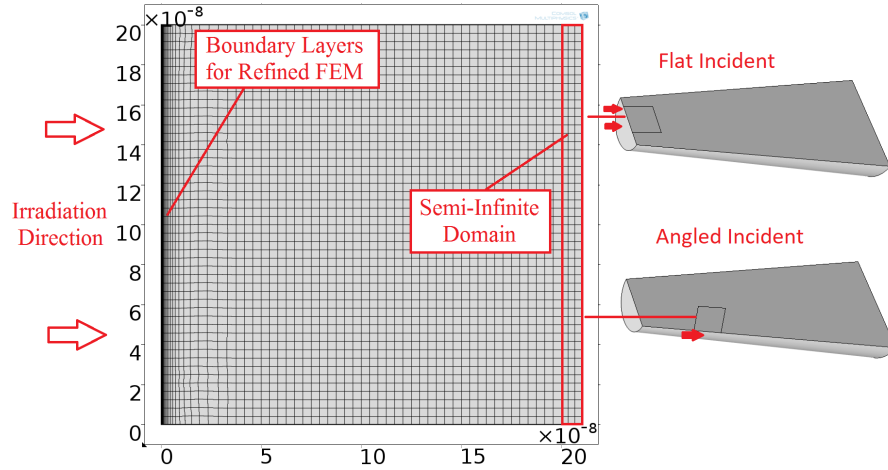


Figure 5: Finite element mesh of the tungsten slab used in COMSOL Rate Theory, where the irradiation direction is shown on the left surface. The deposited Gaussian distribution of helium and FPs is resolved by a fine boundary layer mesh, because of the shallow penetration depth of low energy ions. The right side of the geometry is modeled with semi-infinite domain elements to account for the actual material thickness. Both flat and angled ion incidence are solved using similar mesh, but varied in ion range based on the angle of incidence. The units are given in m.

### 2.3. OKMC Model of Motion and Coarsening

The rate theory presented in the previous section is limited to the representation of the early phases of bubble evolution, where nucleation and individual bubble growth by single atom absorption are dominant. At high helium fluence, however, bubbles near the surface region start to move, and can grow significantly by coalescence. To model these events, we follow our development of the Object Kinetic Monte Carlo (OKMC) model, initially put forth by Sharafat et al. and Takahashi et al. [12, 13]. This OKMC model is described as follows. First, bubbles are introduced in a control volume with a density and an average radius determined by rate theory. Then the time step for random-walk bubble motion is calculated from the diffusion coefficient of bubbles. A single bubble is selected for a jump at each time step. Once the bubble moves the random walk distance, a drift force is applied on it and the bubble is moved along the stress gradient within the same time-step. The entire bubble field is updated for the events of absorption, coalescence, and reaching the control volume boundary. The present procedure builds on our earlier work [12, 13] by adding bubble-to-bubble stress gradient effects, bubble helium and vacancy absorption and trap-mutation effects, and a coalescence based time-stepping scheme.

Without considering external forces due to temperature or stress gradients, bubble diffusion is described by Brownian motion [36]. Both surface- and volume-diffusion of vacancies may operate to move bubbles, but vacancy surface diffusion is the predominant diffusion mechanism for these small bubbles [36–39], and the effective bubble diffusion coefficient can be written as:

$$D_b = \frac{3\Omega^{4/3}}{2\pi R_b^4} D_s \quad (3)$$

where  $D_b$  is the effective bubble diffusion coefficient,  $R_b$  its radius and  $D_s$  is the surface diffusion coefficient, defined as  $D_s = D_0 \exp(-E_s/kT)$ , where  $D_0$  is the pre-exponential and  $E_s$  is the surface activation energy. Surface activation energies and associated pre-exponential factors for tungsten were reported by Ehrlich et al. [35], ranging from 0.92-1.82 eV. This can then be used to relate bubble jump frequency ( $\Gamma_b$ ) and jump distance ( $\lambda_b$ ) as  $D_b = (1/6) \lambda_b^2 \Gamma_b$ . If we make the assumption that the jump distance is to the nearest bubble, a collection of jump frequencies in a control volume can be found. In each OKMC iteration, this collection of jump frequencies are summed and normalized. Then a uniform random number is used to match one of the frequencies as the selection for the current iteration, and its corresponding bubble is chosen for random-walk motion. Next, the time-step for the OKMC iteration is calculated as  $\Delta t = -\ln(RN / \sum \Gamma_b)$ , where  $RN$  is another uniform random number. The Brownian motion is carried out here as a random walk based on this time-step with the given bubble diffusion coefficient, which, in turn, determines its jump frequency  $\Gamma_b$ . Since bubble Brownian motion is driven by surface diffusion, the key factor that determines how far a bubble can move in a given time interval is the self diffusion coefficient. According to the comprehensive review of Ehrlich [35], the activation energy for self diffusion in W is in the range 19-42 kcal/mol (0.92-1.82 eV). The diffusion coefficient pre-factor is in the range  $3.7 \times 10^{-4} - 2 \times 10^{-2} \text{ cm}^2/\text{s}$ . If we take the lower limit of the activation energy, a bubble of 10 nm radius may be able to migrate by random walk more than 500 nm at 1000 K in 1000 s. It is therefore expected that bubble coalescence will take place as a result of random Brownian motion, especially if the bubble density is high where the distance to nearby bubbles is short and can be traveled within the experiment duration.

The influence of stress gradients on bubble migration can be modeled by estimating the Gibb's free energy change in three components: the free energy of the gas in the bubble ( $dG_g$ ), the free energy of system due to a change in the surface area ( $dG_s$ ), and the strain field of the solid ( $dE_{solid}$ ), as outlined by Bullough and Perrin [40]. Assuming a axial stress gradient ( $d\sigma/dx$ ) and ideal gas law, the free energy change of gas in the bubble can be written as  $dG_g = d(pV) - pdV = 0 - pdV = -p(4\pi R_b^2 dR_b)$ , and the free energy change by surface area is  $dG_s = \gamma_b dA = \gamma_b(8\pi R_b dR_b)$ . Taking into account mechanical equilibrium of the gas pressure in bubbles, the hydrostatic component of the stress field is therefore  $\sigma_h = p - (2\gamma_b/R_b)$ , where the internal gas pressure ( $p$ ) is compensated by the bubble's surface tension  $\gamma_b$ . Thus the change in  $R_b$  becomes  $dR_b = -(R_b^2 / (3\sigma_h R_b + 4\gamma_b)) (d\sigma_h/dx) dx$ , which we can use to rewrite  $dG_g$  and  $dG_s$ .

Then by using the elastic energy density from  $\sigma_h$  and the bulk modulus  $K$ ,  $E_{el} = \sigma_h^2/2K$ , the strain energy of the solid can be approximated as the free energy of the matrix minus the elastic energy density from the bubble.  $E_{solid} = E_{solid}^{(0)} - \frac{\sigma_h^2}{2K} \frac{4\pi R_b^3}{3}$ . Taking the derivative with respect to the gradient direction would result in the change in strain field as the function of said gradient. Finally, the total force acting on a bubble would be the sum of all three components

of the free energy change [40], i.e.

$$F_b = -\frac{4\pi R_b^4 \sigma_h}{3\sigma_h R_b + 4\gamma_b} \left(1 - \frac{3\sigma_h R_b + 8\gamma_b}{6R_b K}\right) \left(\frac{d\sigma_h}{dx}\right) \quad (4)$$

The assumption of an axial stress gradient is useful when considering the interaction between two bubbles. The stress gradient on bubbles implies that the unbalanced internal gas pressure by surface tension drives them to move from a lower stress region to a higher one. The total energy decrease is associated with a thermodynamic configurational force that drives the bubble to move. Leiden and Nichols determined that the force between two bubbles of uncompensated internal gas pressure, i.e.  $\sigma_h > 0$ , is always attractive [41]. The attractive force between two bubbles can be estimated from an axial stress gradient along their centers, as we transform the x-axis to coincide with the stress gradient:  $\frac{d\sigma_h}{dx} = (\sigma_h^{(2)} - \sigma_h^{(1)}) / (x_2 - x_1)$ . Then, the velocity of each bubble can be determined as:

$$\vec{v}_b = \frac{D_b}{k_B T} \vec{F}_b \quad (5)$$

in the direction toward the center of the other bubble.

At each OKMC step, the selected bubble for Brownian motion is considered for additional drift motion due to stress gradients. This accounts for the interaction between the selected bubble and all other bubbles within a  $10R_b$  distance [41], in order to reduce the simulation time. All stress gradient related forces here are collected as vectors and summed. The final force vector is used to calculate the velocity of the selected bubble, and the bubble position is then updated. The growth of the bubble due to absorption of surrounding implanted helium and vacancies must also be taken into account. The spatial generation of helium and vacancy during implantation follows are obtained from the spatial rate results and introduced into OKMC simulations. Considering the bubble as a vacancy cluster containing free helium atoms, the absorption of additional vacancies would increase its size, while absorption of helium may force additional trap-mutations to occur. Therefore, the continuous evolution of bubbles must keep track of helium and vacancy count using the last two rate equations (Eq. 2), with the bubble radius directly related to the vacancy count ( $m_2$ ).

When the capture distance between two bubbles overlaps, they coalesce into a larger one. The size of this newly formed bubble can be resolved through two consecutive stages. The first stage assumes that the overall volume of is conserved. i.e.  $V_3 = V_1 + V_2$ , which simplifies to  $R_3^3 = R_1^3 + R_2^3$ . The change in free energy of this stage is negative for all practical cases [36], thus will always occur, and the driving force is generally provided by the reduction in the total surface area. The second stage is volume adjustment that re-establishes the external pressure of the bubble at equilibrium  $p = 2\gamma_b/R_3$ . This would require an increase in gas volume, and an increase in surface area. Thus if one assumes a balance of the ideal gas law during volume adjustment, then the radius of the final bubble can be solved as  $R_3^2 = R_1^2 + R_2^2$ . This signifies that the total surface area after coalescence is the same as before, meaning that the total area decrease in stage I is re-expanded in the same amount in stage II. In low plasma energy exposures, since the internal gas pressure is not fully compensated, i.e.  $\sigma_h > 0$ , we cannot assume stage II to occur, thus only volume conservation is accounted for coalescence in low energy simulations,  $R_3 = \sqrt[3]{R_1^3 + R_2^3}$ . On the other hand, at high implantation energy and sample temperature,

$$R_3 = \sqrt{R_1^2 + R_2^2}.$$

The capture radius of a matrix bubble is calculated using the strain field near the bubble. This distance can be calculated using diffusion limited kinetic theory [42], and Faney et. al. derived this value for a bubble with  $m_1$  helium atom and  $m_2$  vacancies (Eq. 6) [17]. The capture distance of this bubble is independent of helium as its size is only defined by vacancies after trap-mutation. Each additional vacancy introduces a volume increment of  $(a_0^3/2)$  to total volume for a sphere of influence that the bubble's strain field affects. The capture radius of the bubble is given by:

$$r_{He m_1 V m_2} = r_{He 0 V_1} + \left( \frac{3}{4\pi} \frac{a_0^3}{2} m_2 \right)^{1/3} - \left( \frac{3}{4\pi} \frac{a_0^3}{2} \right)^{1/3} \quad (6)$$

where the single vacancy capture radius is defined as  $r_{He 0 V_1} = (\sqrt{3}/4)a_0$  and  $a_0$  is the lattice constant.

Finally, boundary conditions are applied. We assume periodic boundaries on all lateral sides of a cubic volume element bounded by the surface facing the plasma ions, and free exit condition on the plasma-facing surface. In other words, bubbles are released when they intersect the plasma-facing surface. If a bubble leaves the control volume from the entrance surface ( $x = 0$ ), it is removed from the bubble ensemble and added to a list of released bubbles, and its exit location and escape time is recorded. The same procedure is followed if the bubble passes through the control volume ( $x = x_{max}$ ), where the bubble is assumed to penetrate deep into the bulk.

At high plasma ion energy, however, embedded helium clusters are densely populated within the bulk. This leads to a drastic increase in the total number of bubbles in the OKMC model, which can result in unreasonable simulation run-time to resolve time scales comparable to those of typical experiments (i.e. 1000's of seconds). As the distance between bubbles does not increase significantly, the time-step based on random walk alone remains very small. In order to overcome this limitation, an additional implementation is made on the OKMC model via the use of a "coalescence-based" scheme. Using rate theory results as initial conditions, we find the first time-step in which coalescence occurs in the OKMC simulation. The coalescence frequency is the inverse of the average time interval between coalescence events for that average bubble radius and concentration. Next, larger average bubble radii are used to calculate different coalescence rates in OKMC simulations, and the results are curve-fitted to give the coalescence frequency as function of average bubble radius  $P_C(T, R_b)$ , as shown in Figure 6. Thus, the coalescence rate of any bubble can be extrapolated from the curve fit.

A control volume is used here and divided into a number of bins (20 in our case) in the implantation direction, and each bin contains an average bubble radius and concentration calculated again using the rate theory results as initial condition. Here, we use the coalescence rate ( $P_C$ ) instead of the diffusion rate ( $\Gamma_b$ ) as the relevant frequency. The total coalescence rate for each bin is summed, and a uniform random number is used at each iteration step to choose one bin to carry out a coalescence event. This would increase the average bubble radius for that bin while lowering its concentration, effectively giving it a new coalescence rate for the next iteration. Each time-step is calculated as  $\Delta t = -\ln(RN / \sum P_C)$ , where  $RN$  is a uniformly distributed random number.

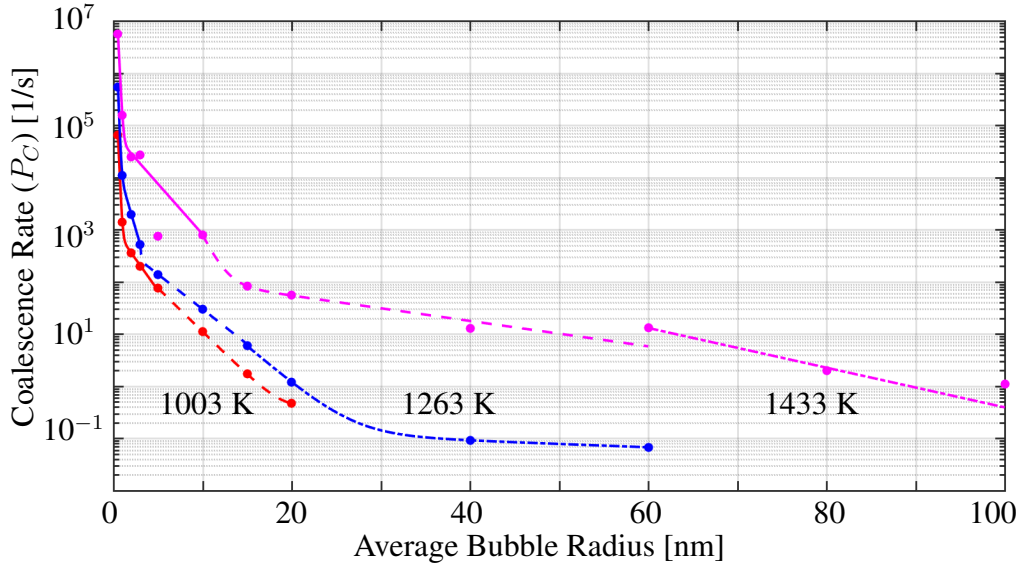


Figure 6: Coalescence rate vs. average bubble radius. The dots are coalescence rates calculated from OKMC based on the given bubble radius at each temperature. Curve fits are made for the coalescence rate and then extrapolated to other bubble radii in the coalescence-based-OKMC. Three second-order exponential fits are made at each temperature in order to more closely fit the coalescence rate determined by OKMC simulations. The curve fits are piecewise continuous to properly represent OKMC data.

### 3. Modeling Results & Comparison with Experiments

#### 3.1. Helium Ion Deposition

The results of Monte Carlo simulations by SRIM are displayed in Figure 7. Each SRIM result shows a backscattering percentage and a probability distribution function resembling a Gaussian. We plotted the mean of that distribution as the ion range at each angle of incidence in 7(b). The simulations indicate that much more ions are backscattered at shallow angles of incidence. These results are consistent with the experimental results conducted at the UCSD PISCES facility with 100 eV helium ions on a micro-pillar covered tungsten surface at 1123 K and  $2 \times 10^{26}$  He<sup>+</sup>/m<sup>2</sup> [5]. The ion penetration depth does not decrease significantly, since low energy helium has shallow deposition in the first place. The peak ion distributions, however, are reduced by up to 50%, because of the high back-scattering coefficient.

#### 3.2. Spatial Rate Theory Results

The spatial distribution of helium implantation calculated by SRIM is fitted to a Gaussian and used as input to the spatially-dependent rate theory, and numerically solved by the finite element method in COMSOL. The peaks are calculated using the ion flux corresponding to the experimental conditions detailed in our recent work [5]. Results of these calculations are shown in Figs. 8 and 9, which display the temporal evolution of bubble concentration near the surface (1 nm) and deeper into the sample (100 nm).

The results clearly show that the bubble density is significantly lower at higher angles of ion incidence. The same trend is also observed for the average bubble radius. The trends are consistent for both near-surface exposure and deep into the sample. To give a feel of the spatial distributions of bubbles, the concentrations of the mobile species (SIAs and helium atoms) near

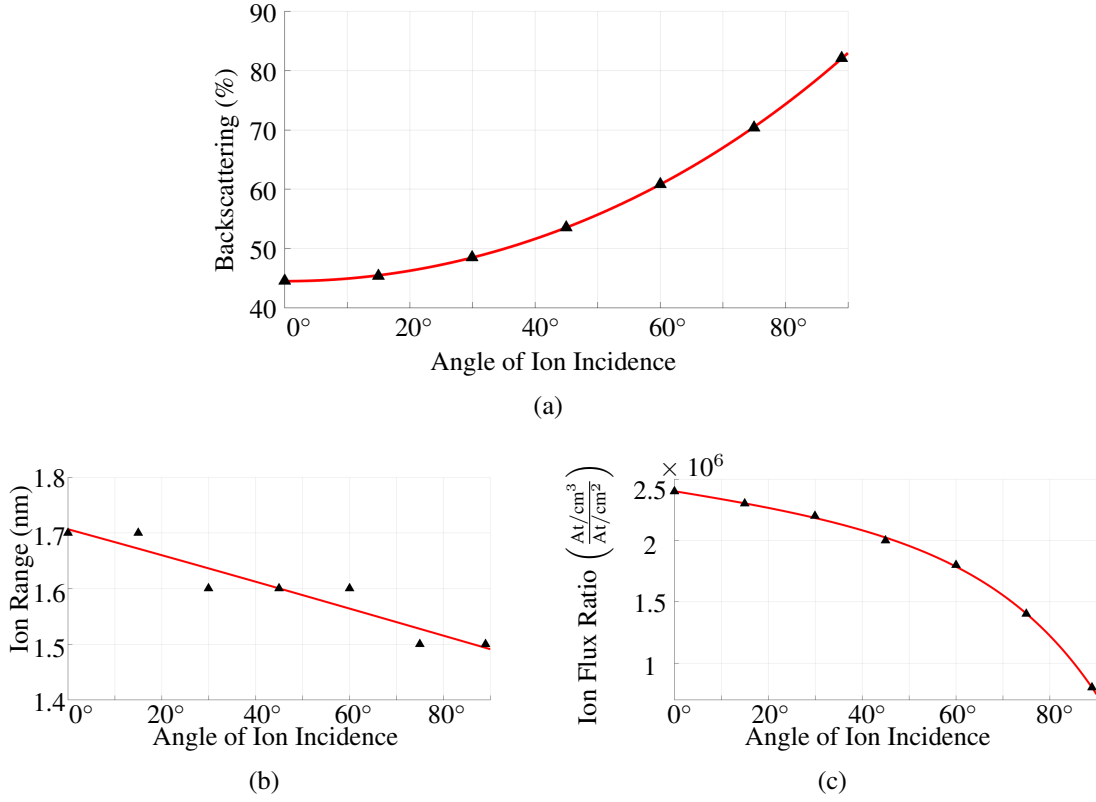


Figure 7: SRIM results for (a) back-scattering coefficient, (b) mean value of ion range, and (c) ion deposition peak for 100 eV helium irradiation on tungsten surface vs. the incident ion angle. The dots represent SRIM results at 15° intervals, while the solid lines represent a curve fit.

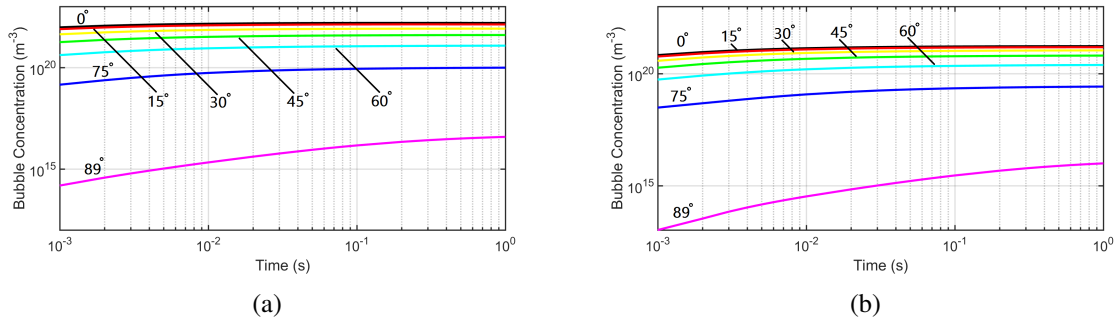


Figure 8: Matrix bubble concentration for 100 eV helium exposure on tungsten at 1123 K at various angle of incidence. (a) at ~1 nm near exposure surface, and (b) at 100 nm.

the surface are shown at 1 second in Figs 10(a) and 10(b), respectively. The corresponding spatial distribution of the bubble concentration and average bubble radius are also shown in Figs 11(a) and 11(b), respectively.

The trends depict strong spatial dependence of bubble concentration and radius as a result of the effect of a free surface on mobile species (helium and SIAs). It is worth noting that the influence of the angle of ion incidence is manifest in the behavior of helium and SIA concentration, as they are directly affected by helium implantation. Furthermore, the vacancy concentration is



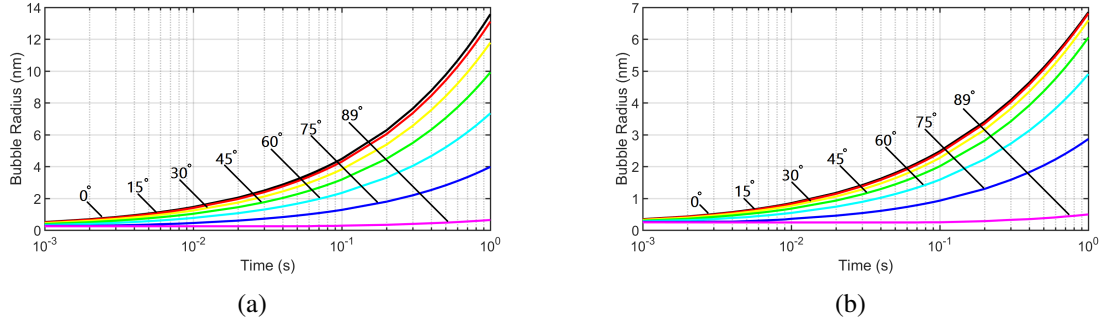


Figure 9: Average matrix bubble radius as function of plasma exposure time for 100 eV helium on tungsten at 1123 K at various angle of incidence. (a) at  $\sim 1$  nm near the exposure surface, and (b) at 100 nm.

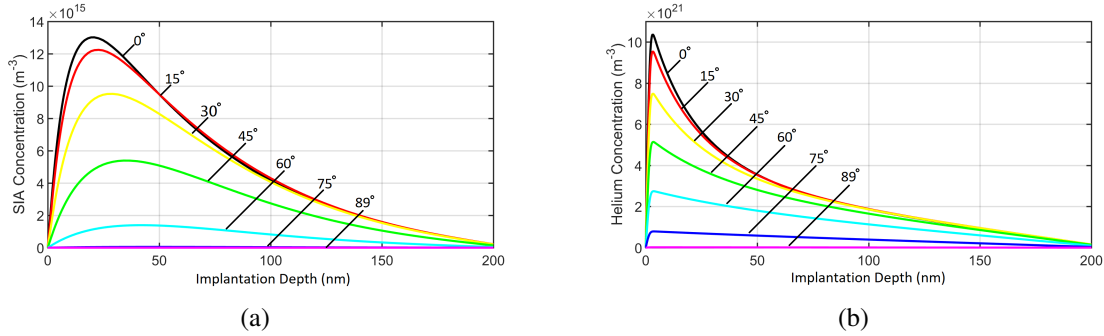


Figure 10: Spatial distribution of mobile single defects for 100 eV helium plasma exposure on tungsten at 1123 K at various angles of ion incidence for (a) SIA concentration, and (b) helium concentration at the final time-step (1s).

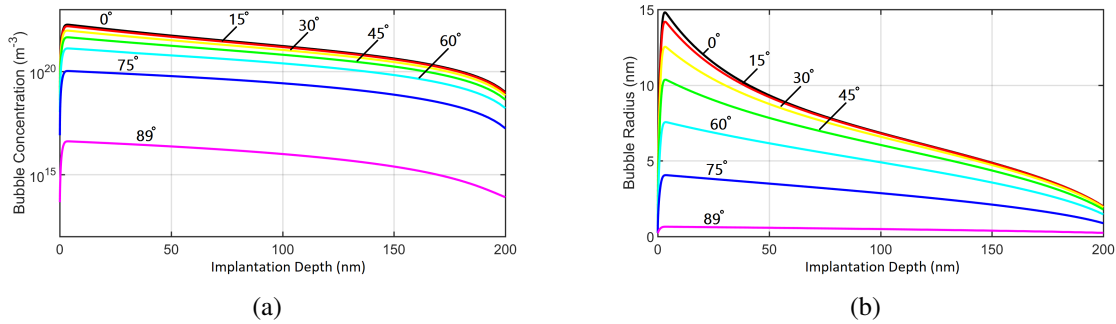


Figure 11: Spatial distribution of bubble density and average radius for 100 eV helium plasma exposure on tungsten at 1123 K at various angles of ion incidence for (a) matrix bubble concentration, and (b) corresponding average radius at the final time-step (1s).

not displayed here since low energy irradiation does not produce vacancies, and thermal vacancies do not have strong spatial effects in the absence of temperature gradients. Bubble growth at low ion implantation energy occurs mainly as a result of trap-mutation rather than vacancy absorption.

### 3.3. OKMC Simulations of Low-Energy Helium Ions

Snapshots of the OKMC model for the planar tungsten case show an initial large concentration of helium bubbles that eventually coalesce into larger sizes, shown in Figure 12. The

bubble concentration ( $C_b$ ), average helium content per bubble ( $m_1$ ), and the average bubble radius ( $R_b$ ) are shown in Table 2. An SEM micro-graph of our experimental results for the helium bubble distribution on the sides of a conical micro-pillar corresponding to an ion incident angle of  $60^\circ$  is shown in Figure 13(a), while the results of the OKMC simulations are shown side-by-side in Figure 13(b). The agreement between theory and experiment is qualitative, given the uncertainties in bubble density estimates between rate theory (high) and OKMC (low due to coalescence). Given that rate theory does not account for whole bubble motion or coalescence, OKMC simulations provide a crucial role in determining the coarsening mechanisms that control final bubble size and density at longer timescales.

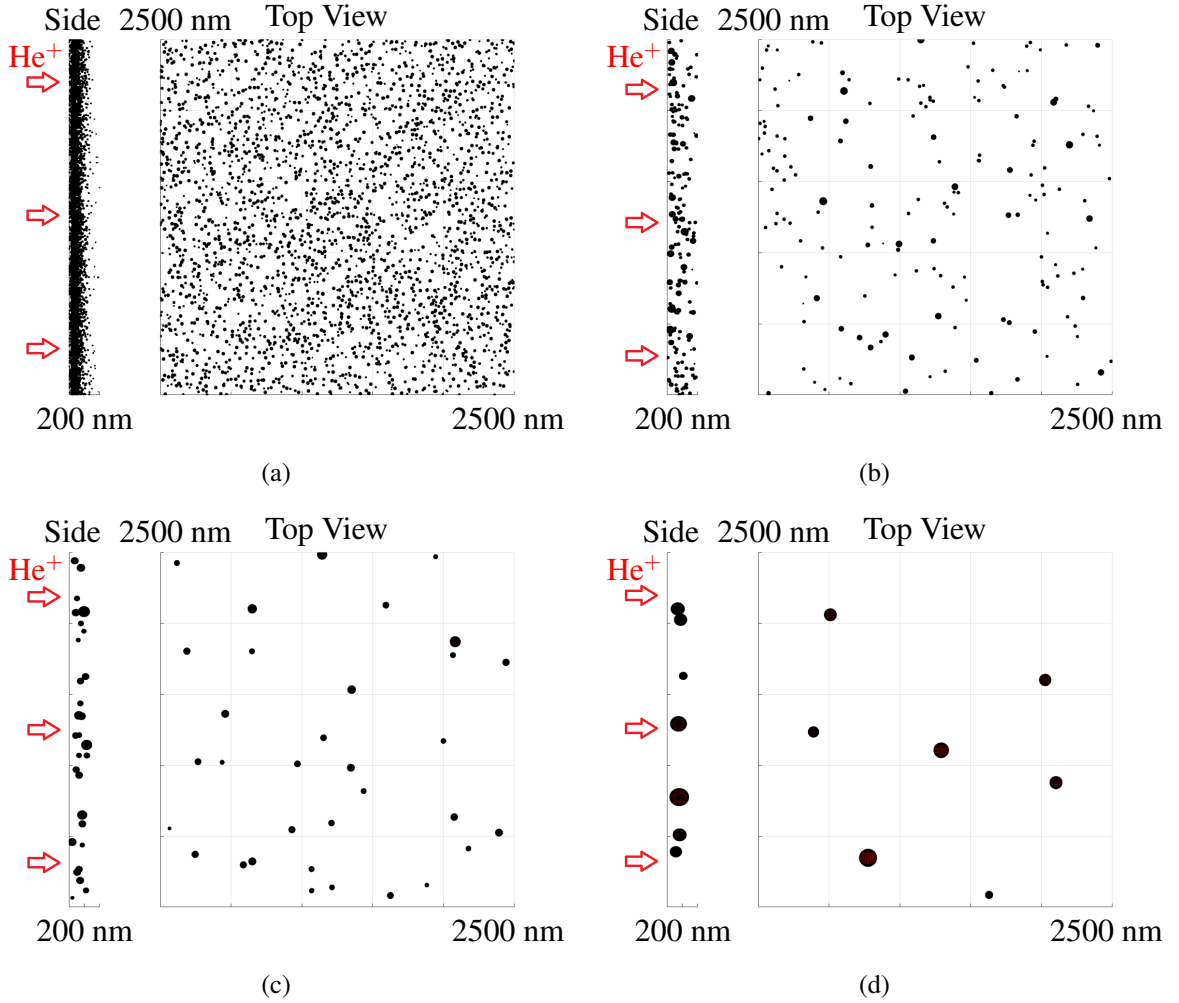


Figure 12: OKMC snapshots of helium bubbles at  $0^\circ$  angle of ion incidence within the control volume of  $2500 \text{ nm} \times 2500 \text{ nm} \times 200 \text{ nm}$ . Side and top views are shown in (a) 1s (Rate Theory Results), (b) 60s, (c) 300s, (d) 1800s.

OKMC simulation results for low-energy helium plasma show that the angle of ion incidence plays a significant role on bubble formation. It is interesting to note that the bubble concentration peaks around an incidence angle of  $60^\circ$ , as can be seen in Figure 14(a). As the incidence angle increases, the depth of penetration decreases and the ion backscattering coefficient increases. This leads to a drop in the overall bubble concentration as calculated in rate theory (Figure 8 and 11(a)). This concentration is in turn the controlling factor for the coales-

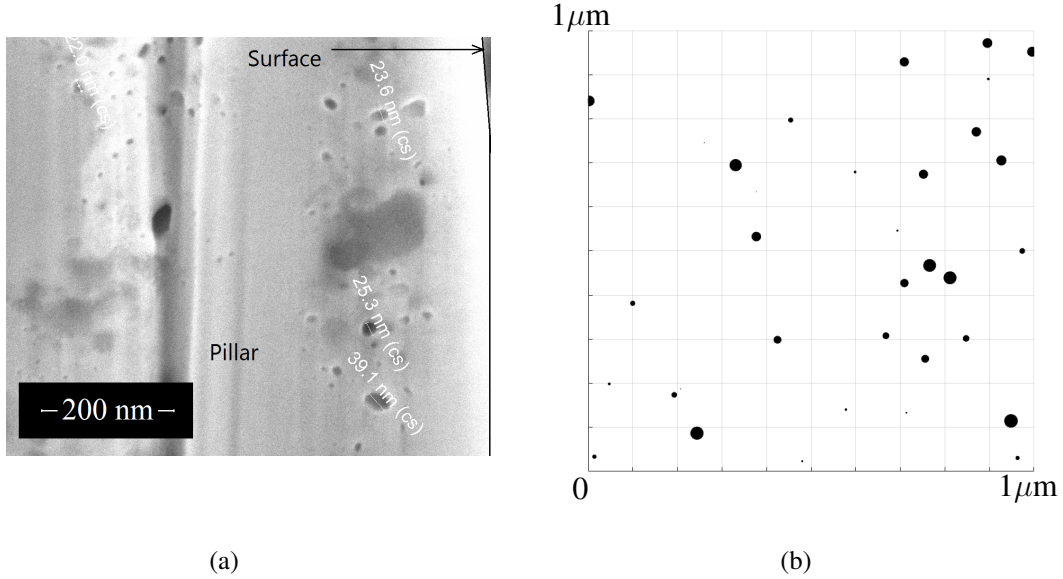
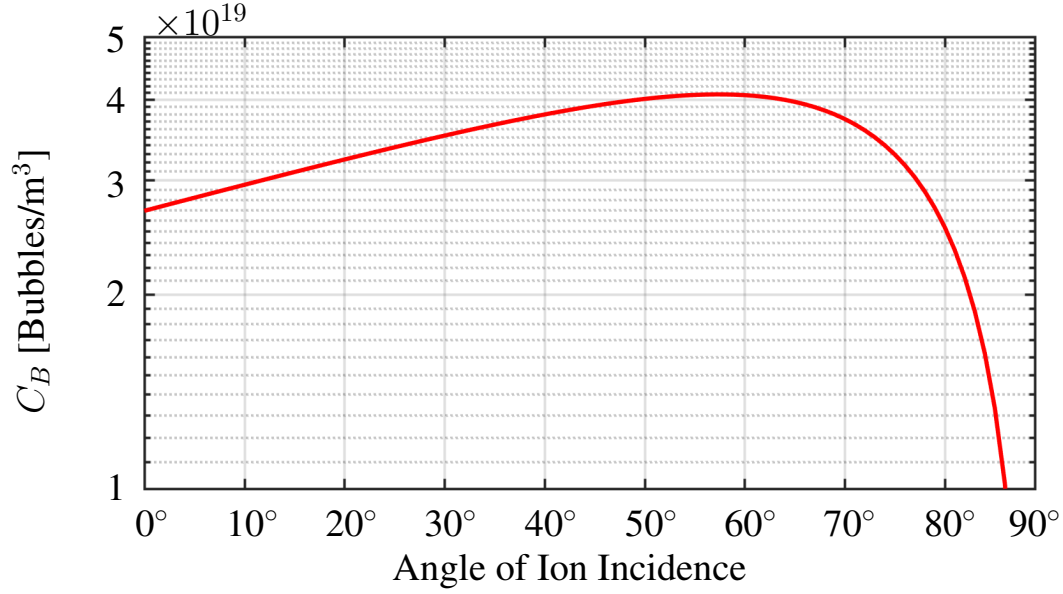


Figure 13: Comparison between modeling and experiments of 100 eV helium plasma ion exposure on tungsten. (a) SEM image of the cross-section of a micro-pillar with pillar surface to the right [5] and (b) OKMC simulation results of a similar configuration at 60° angle of ion incidence.

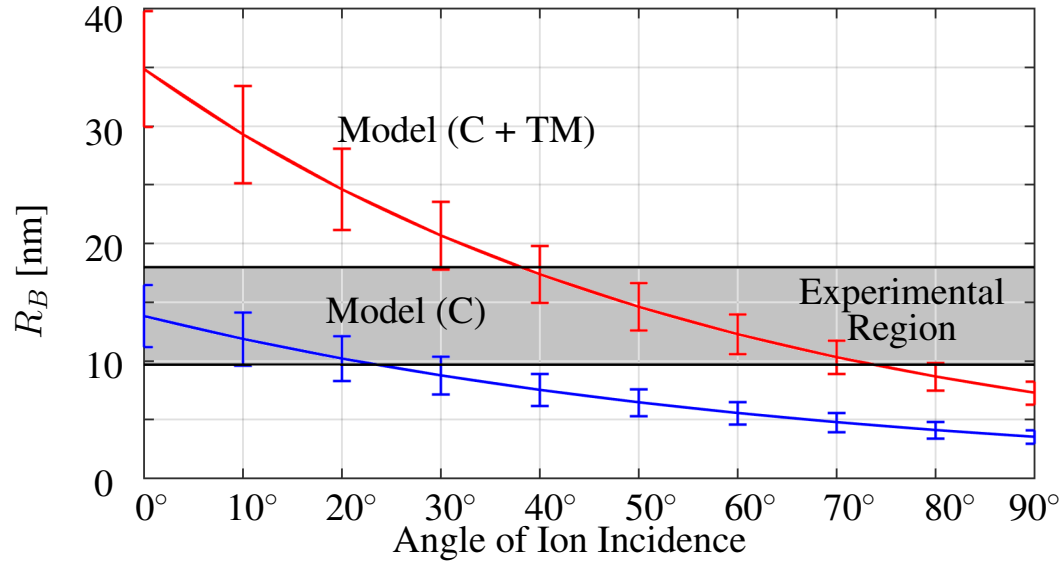
| Incident angle | $C_b$ ( $m^{-3}$ )    | $m_1$ (atom/bubble)                     | $R_b$ (nm)          |
|----------------|-----------------------|---|---------------------|
| 0°             | $3.10 \times 10^{19}$ | $2.98 \times 10^7 \pm 1.30 \times 10^7$ | $29.82 \pm 4.21$    |
| 15°            | $3.09 \times 10^{19}$ | $2.89 \times 10^7 \pm 1.31 \times 10^7$ | $29.50 \pm 4.22$    |
| 30°            | $3.07 \times 10^{19}$ | $2.18 \times 10^7 \pm 9.64 \times 10^6$ | $26.88 \pm 3.70$    |
| 45°            | $3.02 \times 10^{19}$ | $1.10 \times 10^7 \pm 4.69 \times 10^6$ | $21.46 \pm 2.89$    |
| 60°            | $5.58 \times 10^{19}$ | $1.37 \times 10^6 \pm 7.19 \times 10^5$ | $10.58 \pm 1.83$    |
| 75°            | $2.62 \times 10^{19}$ | $1.09 \times 10^5 \pm 2.15 \times 10^4$ | $4.67 \pm 0.31$     |
| 89°            | $1.02 \times 10^{10}$ | $369 \pm 11$                            | $0.705 \pm 0.00729$ |
| Experiment     | $4.04 \times 10^{20}$ | -                                       | $13.80 \pm 4.15$    |

Table 2: OKMC simulation results for bubble concentration, average helium content, and average bubble radius after 1800 s (30 min). Experimental data on micro-pillar tungsten conducted at the UCSD’s PISCES-B facility are also shown for comparison [5]. The 60° results are highlighted since it is the closest simulation results compared to experimental one.

cence rate in subsequent OKMC simulations. At angles steeper than 60° incidence, the initial bubble concentration calculated from rate theory is too low to play an effect on coalescence. Therefore, a drop-off in the final bubble concentration during OKMC is observed at angles steeper than 60°. The interplay between these two factors leads to a maximum at 60°. This is consistent with our experimental results showing that the sides of cylindrical micro-pillars are free of W fuzz [5]. The computed average bubble radius is in general agreement with the experimental results for angle of ion incidence above 30°. In the angle of ion incidence range of 45° to 60°, the simulation results are the closest to experimental measurements [5], within 1-2 standard deviations of the experimental average. However, the simulation results underestimate



(a)



(b)

Figure 14: (a) OKMC bubble concentration results as a function of angle of ion incidence for 100 eV helium ion irradiation on a tungsten surface. (b) Final average bubble radius with standard deviations vs. angle of ion incidence with coalescence(C), and with coalescence plus trap mutation (C + TM). The results are also compared with experimental data in the gray region for 100 eV helium plasma exposure on micro-pillar tungsten [5], this region depicts the average bubble radius  $\pm$  its standard deviation.

the bubble density as compared to experimental values because of the larger control volume in the simulation as compared to the experiment.

Figure 14(b) shows that trap mutation and coalescence together are necessary processes for the simulated bubble size to be comparable to the experimental values. The results for bubble coalescence alone underestimates the average bubble radius by roughly half as compared to our experimental results [5]. These results indicate that trap mutation is an important mechanism for bubble growth in low-energy helium plasma implantation. Since vacancy production is limited at 100 eV helium ion energy (the PKA energy is below the displacement threshold for W). Vacancies are created when SIAs are kicked out of the bubble volume to balance the expanding internal gas pressure. Ejected SIA's accumulate near the surface to create the nano-meter fuzz structure that is often observed experimentally [2].

### 3.4. OKMC Simulations of High-Energy Helium Ions

At high helium ion energy, the penetration depth in W is much deeper than at low-energy, and experimental observations show that the surface of W becomes porous above 1000 K due to large bubbles in the sub-surface region [6]. The multiscale model was used to simulate bubble formation in W for 30 keV helium ions incident on a flat surface at 1003 K, 1263 K, and 1433 K in order to compare to high energy experimental results from UW-Madison [6, 12]. Surface pore formation started just below  $4 \times 10^{16}$  He+/cm<sup>2</sup>, while the pore size increased and the pore density decreased with increasing fluence and temperature. Snapshots of the OKMC model for 1263 K are shown in Figure 15. Table 3 gives the simulation results for the bubble concentration ( $C_b$ ), average helium content per bubble ( $m_1$ ), and the average bubble radius ( $R_b$ ) corresponding to the experiments.

Time evolution of simulated bubble radius at each temperature is shown and compared with experimental results at the final time-step in (Figure 16). The lowest temperature case (1003 K) slightly overestimates the radius while the other two cases (1263 K, 1433 K) are both on-par with experimental radius. This is notable since the higher temperature cases are exposed to higher ion flux over lower total time to maintain similar fluence; thus temperature gradient which was neglected in the model may play a small role in the discrepancy. The standard deviation of the high energy simulations are considerably smaller due to the bin size chosen from the rate theory results. We chose large bin size for this calculation to reduce the simulation time, more variance in the average bubble size can be obtained with smaller bin size, but simulations would be considerably longer.

| Temperature | Type       | $C_b$ (m <sup>-3</sup> ) | $m_1$ (Helium/Bubble) | $R_b$ (nm)        |
|-------------|------------|--------------------------|-----------------------|-------------------|
| 1003 K      | Experiment | $3.92 \times 10^{21}$    | -                     | $20.33 \pm 2.51$  |
|             | Simulation | $9.51 \times 10^{20}$    | $2.14 \times 10^4$    | $24.75 \pm 0.37$  |
| 1263 K      | Experiment | $2.67 \times 10^{20}$    | -                     | $56.27 \pm 11.44$ |
|             | Simulation | $1.24 \times 10^{20}$    | $1.37 \times 10^5$    | $53.21 \pm 0.65$  |
| 1433 K      | Experiment | $1.66 \times 10^{19}$    | -                     | $88.00 \pm 20.02$ |
|             | Simulation | $5.04 \times 10^{19}$    | $5.32 \times 10^5$    | $79.34 \pm 0.36$  |

Table 3: Comparison of OKMC simulation results for average bubble radius and concentration to experimental values conducted at the University of Wisconsin-Madison [6].

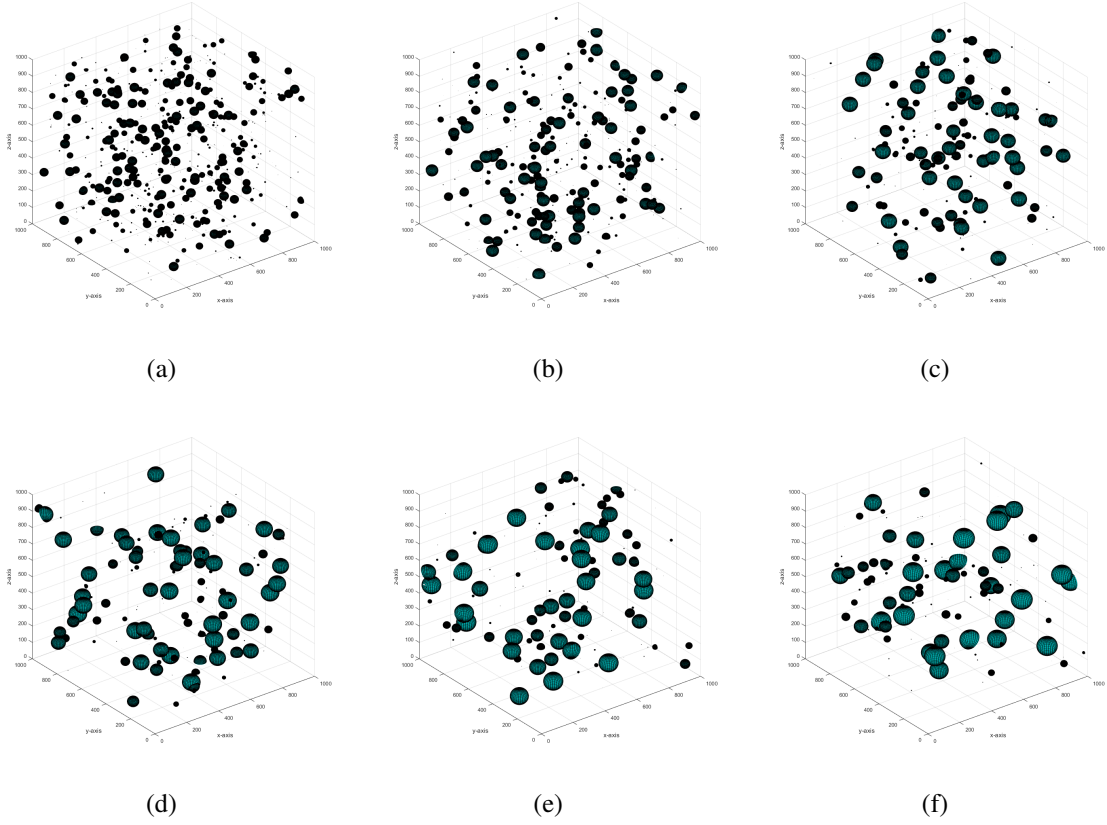


Figure 15: Coalescence based KMC snapshots of helium bubbles at 30 keV incident ion energy at 1263 K within a control volume of  $1 \mu\text{m} \times 1 \mu\text{m} \times 1 \mu\text{m}$  at (a) 1s (Rate Theory Results), (b) 90 s, (c) 180 s, (d) 270 s, (e) 360 s, (f) 450 s.

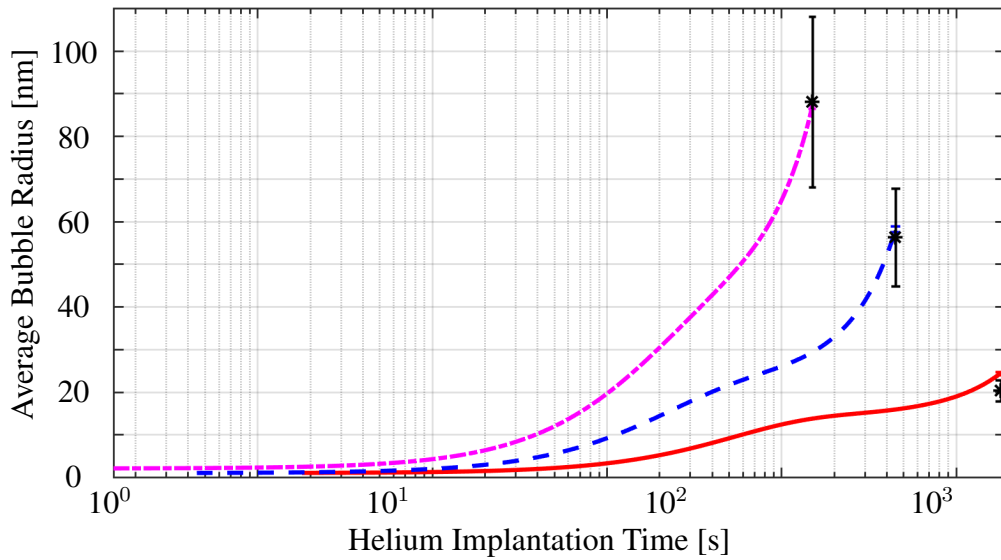


Figure 16: Average bubble radius evolution from coalescence based OKMC for (—) 1003 K, (---) 1263 K, (-.-) 1433 K. Experimental results from UW-Madison [12] are also shown in (\*) along with their standard deviations.

The coalescence based KMC simulation results for the high energy case show that the average bubble radius closely matches the experimental values. The simulation radius are within 9.8% at 1003 K, 2.8% at 1263 K, and 5.2% at 1433 K from the corresponding experimental values. However, the agreement between simulation and experiment concentration is only qualitative, with associated differences of 61.0% at 1003 K, 36.6% at 1263 K, and 50.4% at 1433 K. A comparison between experimental surface hole pattern and the simulation results is shown in Figure 17. The simulation results at different temperatures are consistent with experimental data, as shown in Figure 16. The two higher temperature cases exhibit simulated bubble radii within only one standard deviation of the experimental average, while the lower temperature case exhibits at most two standard deviations. The average bubble size increases with temperature in the range 1000 K to 1400 K. At high temperature and ion energy, the abundance of vacancies produced by ion collision cascades allow bubbles to be in equilibrium with the internal gas pressure, diminishing the role of trap mutation. Thus, the main mechanism of bubble growth during high energy irradiation is coalescence. In the high energy case, there were ample vacancies that were produced by irradiation which can be clearly seen in rate theory results. These high vacancy concentrations were passed on to the OKMC simulations where even though the trap-mutation mechanism was turned on in the code, actual events were not triggered. Bubbles tended to grow from vacancy absorption fast enough that the internal gas pressure was equilibrated by external surface tension. Similarly, the bubble-to-bubble stress gradient effect was negligible since the uncompensated gas pressure in bubbles was nearly zero.

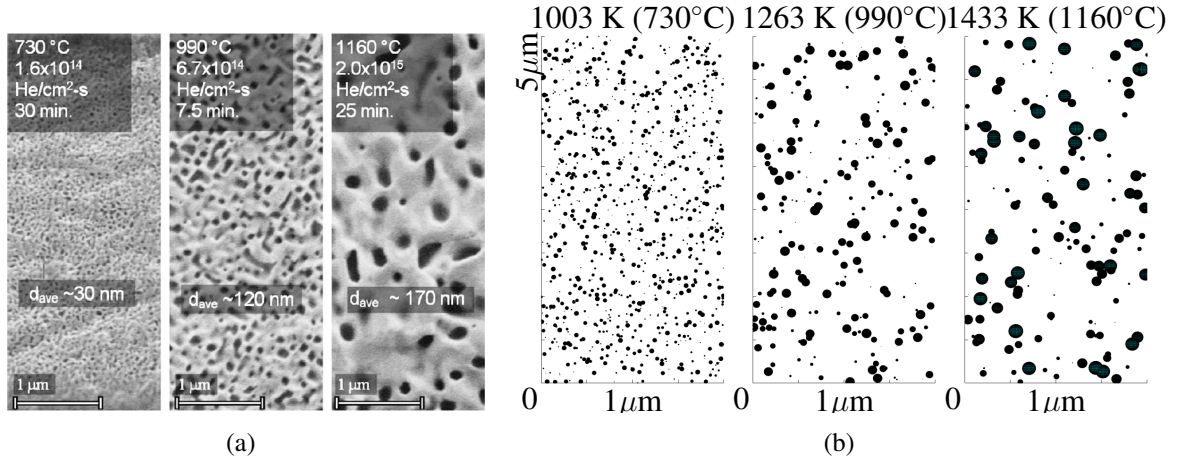


Figure 17: Comparison of 30 keV helium ion exposure on tungsten between (a) experimental results from Wisconsin Madison [6] and (b) coalescence based OKMC simulation resultant surface holes. The SEM micro-graph in Fig. (a) is obtained by permission.

#### 4. Conclusions

The developed multiscale framework for the simulation of helium bubbles in plasma-irradiated W was able to capture the entire evolution process over experimental time scales (e.g. 30 minutes for 100 eV helium ion irradiation on angled tungsten surfaces). Past modeling attempts, such as molecular dynamics, cluster dynamics, and Monte Carlo have been limited to modeling either incubation, nucleation, or growth of these helium bubbles, but not the entire process. By



applying the multiscale approach, we were able to simulate the behavior of subsurface bubbles in tungsten.

Application of the multiscale model to low-energy helium ion irradiation of micro-engineered W, where the sample surface is covered with a dense forest of W micro-pillars revealed the important effects of ion incidence angle on bubble evolution. It is found that at steep angles (measured from surface normal) of ion incidence, the backscattering coefficient becomes so large, and the implantation depth so shallow that virtually no bubbles form near the surface. This is consistent with our experimental observations of the lack of bubbles or fuzz on the sides of cylindrical pillars exposed to low-energy plasma [5]. The predicted average bubble radius is found to be within 26.0% - 44.2% of experimental observations, and the concentration is on the same order of magnitude. Furthermore, the model shows that the mechanism of trap-mutation is the main controlling factor in bubble growth during low energy helium exposure.

At high helium ion energy (e.g. 30 keV), the mechanism of trap-mutation ceases to be important because of the abundance of vacancies produced by collision cascades. The average bubble radius was found to be close to experimental data at three different temperature and fluence; the difference being in the range 2.8% to 9.8%. However, the bubble concentrations are over-estimated by 36.6% - 61.0%. It is confirmed that at high-energy and at temperatures above 1000 K, the key mechanism of bubble growth is by coalescence. The coalescence process is modeled by an elastic interaction that drives nearby bubbles to move towards one another to reduce energy. Large bubbles resulting from coalescence are found to be in thermodynamic equilibrium achieved between the internal pressure and the surface tension. The closeness of such large bubbles to the surface results in the porous structure that is experimentally observed.

## Acknowledgments

The authors wish to acknowledge the support of the U.S. Department of Energy, Office of Fusion Energy, through the DOE award number DE-SC0018410 at UCLA.

## References

- [1] G. Janeschitz, I. JCT, et al., Plasma-wall interaction issues in iter, *Journal of Nuclear Materials* 290 (2001) 1–11.
- [2] Y. Ueda, H. Peng, H. Lee, N. Ohno, S. Kajita, N. Yoshida, R. Doerner, G. De Temmerman, V. Alimov, G. Wright, Helium effects on tungsten surface morphology and deuterium retention, *Journal of Nuclear Materials* 442 (1-3) (2013) S267–S272.
- [3] K. Wang, R. Doerner, M. J. Baldwin, F. W. Meyer, M. E. Bannister, A. Darbal, R. Stroud, C. M. Parish, Morphologies of tungsten nanotendrils grown under helium exposure, *Scientific reports* 7 (2017) 42315.
- [4] G. Z. Li, T. S. Matlock, D. M. Goebel, C. A. Dodson, C. S. Matthes, N. M. Ghoniem, R. E. Wirz, In situ plasma sputtering and angular distribution measurements for structured molybdenum surfaces, *Plasma Sources Science and Technology* 26 (6) (2017) 065002.
- [5] E. Gao, W. Nadvornick, R. Doerner, N. M. Ghoniem, The influence of low-energy helium plasma on bubble formation in micro-engineered tungsten, *Journal of Nuclear Materials*.



- [6] B. Cipiti, G. Kulcinski, Helium and deuterium implantation in tungsten at elevated temperatures, *Journal of nuclear materials* 347 (3) (2005) 298–306.
- [7] H. Trinkaus, B. Singh, Helium accumulation in metals during irradiation—where do we stand?, *Journal of Nuclear Materials* 323 (2-3) (2003) 229–242.
- [8] J. Boisse, C. Domain, C. Becquart, Modelling self trapping and trap mutation in tungsten using dft and molecular dynamics with an empirical potential based on dft, *Journal of Nuclear Materials* 455 (1-3) (2014) 10–15.
- [9] J. F. Ziegler, M. D. Ziegler, J. P. Biersack, Srim—the stopping and range of ions in matter (2010), *Nuclear Instruments and Methods in Physics Research Section B: Beam Interactions with Materials and Atoms* 268 (11-12) (2010) 1818–1823.
- [10] N. M. Ghoniem, J. N. Alhajji, D. Kaletta, The effect of helium clustering on its transport to grain boundaries, *Journal of Nuclear Materials* 136 (2-3) (1985) 192–206.
- [11] N. Ghoniem, Nucleation and growth theory of cavity evolution under conditions of cascade damage and high helium generation, *Journal of nuclear materials* 174 (2-3) (1990) 168–177.
- [12] S. Sharafat, A. Takahashi, K. Nagasawa, N. Ghoniem, A description of stress driven bubble growth of helium implanted tungsten, *Journal of Nuclear Materials* 389 (2) (2009) 203–212.
- [13] A. Takahashi, S. Sharafat, K. Nagasawa, N. Ghoniem, Kinetic monte carlo simulation of helium-bubble evolution in ods steels, in: *Effects of Radiation on Nuclear Materials and the Nuclear Fuel Cycle: 24th Volume*, ASTM International, 2010.
- [14] C.-C. Fu, F. Willaime, Interaction between helium and self-defects in  $\alpha$ -iron from first principles, *Journal of Nuclear Materials* 367 (2007) 244–250.
- [15] W. Wilson, C. Bisson, M. Baskes, Self-trapping of helium in metals, *Physical Review B* 24 (10) (1981) 5616.
- [16] J. Evans, A. Van Veen, L. Caspers, Direct evidence for helium bubble growth in molybdenum by the mechanism of loop punching, *Scripta Metallurgica* 15 (3) (1981) 323–326.
- [17] T. Faney, Numerical simulations of tungsten under helium irradiation, Ph.D. thesis, University of California, Berkeley (2013).
- [18] C. S. Becquart, C. Domain, U. Sarkar, A. Debacker, M. Hou, Microstructural evolution of irradiated tungsten: Ab initio parameterisation of an okmc model, *Journal of nuclear materials* 403 (1-3) (2010) 75–88.
- [19] Y. Li, W. Zhou, L. Huang, Z. Zeng, X. Ju, Cluster dynamics modeling of accumulation and diffusion of helium in neutron irradiated tungsten, *Journal of Nuclear Materials* 431 (1-3) (2012) 26–32.
- [20] D. Nguyen-Manh, A. Horsfield, S. Dudarev, Self-interstitial atom defects in bcc transition metals: Group-specific trends, *Physical Review B* 73 (2) (2006) 020101.

- [21] M. A. El Keriem, D. Van Der Werf, F. Pleiter, Helium-vacancy interaction in tungsten, *Physical review B* 47 (22) (1993) 14771.
- [22] D. Nguyen-Manh, S. Dudarev, Trapping of he clusters by inert-gas impurities in tungsten: First-principles predictions and experimental validation, *Nuclear Instruments and Methods in Physics Research Section B: Beam Interactions with Materials and Atoms* 352 (2015) 86–91.
- [23] C. Becquart, C. Domain, An object kinetic monte carlo simulation of the dynamics of helium and point defects in tungsten, *Journal of Nuclear Materials* 385 (2) (2009) 223–227.
- [24] N. Juslin, B. Wirth, Interatomic potentials for simulation of he bubble formation in w, *Journal of Nuclear Materials* 432 (1) (2013) 61–66.
- [25] L.-F. Wang, X. Shu, G.-H. Lu, Comparison of two tungsten–helium interatomic potentials, *Journal of Materials Research* 30 (9) (2015) 1464–1472.
- [26] S. Sharafat, N. Ghoniem, Comparison of a microstructure evolution model with experiments on irradiated vanadium, *Journal of nuclear materials* 283 (2000) 789–793.
- [27] G. Williamson, R. Smallman, Iii. dislocation densities in some annealed and cold-worked metals from measurements on the x-ray debye-scherrer spectrum, *Philosophical Magazine* 1 (1) (1956) 34–46.
- [28] J. Marian, T. L. Hoang, Modeling fast neutron irradiation damage accumulation in tungsten, *Journal of Nuclear Materials* 429 (1-3) (2012) 293–297.
- [29] Q. Hu, S. Sharafat, N. M. Ghoniem, Modeling space-time dependent helium bubble evolution in tungsten armor under ife conditions, *Fusion Science and Technology* 52 (3) (2007) 574–578.
- [30] J. Yntema, W. Schneider, Compressibility of gases at high temperatures. iii. the second virial coefficient of helium in the temperature range 600 c to 1200 c, *The Journal of Chemical Physics* 18 (5) (1950) 641–646.
- [31] J. E. Kilpatrick, W. E. Keller, E. F. Hammel, Second virial coefficients of helium from the exp-six potential, *Physical Review* 97 (1) (1955) 9.
- [32] G. Garberoglio, A. H. Harvey, First-principles calculation of the third virial coefficient of helium, *Journal of research of the National Institute of Standards and Technology* 114 (5) (2009) 249.
- [33] H. Boschi-Filho, C. Butters, Second virial coefficient for real gases at high temperature, *arXiv preprint cond-mat/9701185*.
- [34] J. Barbour, F. Charbonnier, W. Dolan, W. Dyke, E. Martin, J. Trolan, Determination of the surface tension and surface migration constants for tungsten, *Physical Review* 117 (6) (1960) 1452.

- [35] G. Ehrlich, Direct observations of the surface diffusion of atoms and clusters, *Surface Science* 246 (1-3) (1991) 1–12.
- [36] F. Nichols, Kinetics of diffusional motion of pores in solids: A review, *Journal of Nuclear Materials* 30 (1-2) (1969) 143–165.
- [37] R. Kelly, Bubble diffusion and the motion of point defects near surfaces.(diffusion theory for discrete media, part iv, *physica status solidi (b)* 21 (2) (1967) 451–459.
- [38] P. Goodhew, S. Tyler, Helium bubble behaviour in bcc metals below  $0.65t_m$ , in: *Proceedings of the Royal Society of London A: Mathematical, Physical and Engineering Sciences*, Vol. 377, The Royal Society, 1981, pp. 151–184.
- [39] J. Evans, R. E. Galindo, A. van Veen, A description of bubble growth and gas release during thermal annealing of helium implanted copper, *Nuclear Instruments and Methods in Physics Research Section B: Beam Interactions with Materials and Atoms* 217 (2) (2004) 276–280.
- [40] R. Bullough, R. Perrin, Growth, stability, and interactions of voids and gas bubbles in solids., Tech. rep., Atomic Energy Research Establishment, Harwell, Eng. (1969).
- [41] S. Leiden, F. Nichols, Influence of stress interaction effects upon pore motion in solids, *Journal of Nuclear Materials* 38 (3) (1971) 309–318.
- [42] T. Waite, Theoretical treatment of the kinetics of diffusion-limited reactions, *Physical review* 107 (2) (1957) 463.